Far-Field Wake-Vortex Characteristics of Wings

D. L. Ciffone* and K. L. Orloff†
NASA Ames Research Center, Moffett Field, Calif.

Velocity measurements have been made in the wake of wings that were being towed underwater. As the wake aged, measurements of the tangential and axial velocity profiles were made with a two-dimensional scanning laser velocimeter at downstream distances of 5 to 200 span lengths behind wings with different span loadings. The results identify two characteristic flow regions for the dependence of vortex maximum tangential velocity on downstream distance. The first, a region with little, if any, change in maximum tangential velocity, extends from wake rollup to downstream distances as great as 100 span lengths, depending on span loading and angle of attack. This is followed by a decay region in which the maximum tangential velocity decreases with downstream distance at rates nominally proportional to the inverse one-half power. It is shown that tailoring the wingspan loading by either planform or flap deflection can reduce the maximum vortex tangential velocity by a factor of 2 and thus broaden the vortex core. Vortex mutual interactions and instabilities were introduced by alternate up-down flap deflections, delaying vortex rollup to downstream distances of 45 spans.

Nomenclature

Å = angstrom, units of wavelength (10^{-8} cm)
Æ = aspect ratio
b = wing span
b_e = vortex span
c = wing reference chord
c' = wing chord
C_D = drag coefficient
C_ℓ = section lift coefficient
C_L = lift coefficient
f_x = LV signal frequency for horizontal velocity component
f_z = LV signal frequency for vertical velocity component
LV = laser velocimeter
q = dynamic pressure
r = radial distance from vortex centerline
r_1 = radius of maximum tangential velocity
Re_c = Reynolds number based on wing chord
S = wing area
u = vortex velocity component parallel to tank centerline
U_∞ = towing speed
V_θ = vortex tangential velocity component
V_x = vortex axial velocity component
w = vortex velocity component normal to tank centerline
x = downstream distance, aft from trailing edge of wingtip
α = angle of attack
Γ_0 = circulation shed from one side of wing = $(1/2)(C_L/Æ)(b/b_e)U_\infty b$
η = percent span, y/b
θ = intersection angle of the crossed laser beams
μ = index of refraction

Presented at the AIAA 7th Fluid and Plasma Dynamics Conference, Palo Alto, California, June 17-19, 1974; submitted June 21, 1974; revision received October 29, 1974. The author wishes to thank M. Kelly, Chief of the Large Scale Aerodynamics Branch at the NASA Ames Research Center for many helpful suggestions and discussions, and also O. Lemmer for valuable assistance in data reduction.

Index categories: Jets, Wakes, and Viscid-Inviscid Flow Interactions; Aircraft Aerodynamic (Including Component Aerodynamics).

*Research Scientist.
†Research Scientist. Member AIAA.

Introduction

LIFT-generated wake vortices trailing behind present-day heavy aircraft are currently of great concern to the aviation community. In order to minimize the upset potential which these vortices present to following aircraft, an undertanding of the wake characteristics in the far field, where such encounters are likely to occur is required. Inviscid calculations by Rossow [1] suggest that modification to the span loading of a given wing can significantly reduce the wake-vortex rotational velocities and, for certain loadings, actually inhibit rollup of the vortex sheet into organized vortices. Experimental verification of these concepts has not, however, been reported.

Available wind-tunnel data on vortex axial and tangential velocity profiles are limited by the physical lengths of tunnel test sections. Maximum downstream distances of 30 span lengths have been obtained in the NASA Ames 40- by 80 ft Wind Tunnel. [2] At these distances, however, the characteristics of the vortex decay cannot be established. What is lacking are measured velocity profiles which describe the wake structure from several span lengths to hundreds of span lengths. An integration of the measured tangential velocities across the wingspan of encountering aircraft would then allow an evaluation of the ability to recover from a vortex induced upset at any downstream location.

The purpose of the present investigation was to obtain a complete description of the downstream development of the wake vortex to a distance of several hundred spans and to evaluate the effects of wing angle of attack and span loading on the far-field vortex characteristics. Tests were performed in the University of California's water towing-tank facility at Richmond, Calif. Test Reynolds number based on wing chord was 2.4×10^5. Time-dependent velocity distributions in the wakes of 0.61m (2 ft) span rectangular, diamond, and swept-wing planforms were measured by using the two-dimensional scanning laser velocimeter instrument discussed in Refs. 3-6. Flap deflections on the swept-wing planform allowed additional span-load modifications to be investigated. Data were obtained at downstream distances of $5 \leq x/b \leq 200$.

Experimental Apparatus and Procedure

The test facility was the University of California's water tow-tank located in Richmond, California. The tank is 61m long, 2.44m wide, and 1.7m deep. However, only a 35m

length was utilized. The test section was located approximately 14m from the starting point of the carriage and 21m from the stopping location. Large glass windows at the test section extend from a point approximately 0.6m above the bottom of the tank to well above the free surface (Fig. 1). The carriage, from which the models and connecting strut were suspended, is electrically driven and capable of a maximum speed of just over 2 m/sec. A photosensitive timing system mounted on the carriage structure provides for an accurate readout of the carriage speed which was 2.07 m/sec for this sequence of tests.

Wings and Strut

The length of the streamlined strut to which the models were mounted was such that the trailing edge of the wing was 0.7m above the bottom of the tank (1m below the free surface). Angles of attack were set by using machined wedges at the attachment point at the top of the strut. In addition, the wings were installed in an inverted position so that the vortex pair would rise toward the free surface as they aged, allowing better visualization.

In the first sequence of tests, it was decided to separate pure span-loading effects from turbulent effects. Simple wing planforms were used to obtain different span-load distributions, as opposed to the use of deflected surfaces with one common planform. The planforms chosen were the rectangular, diamond, and sweptwings described in Table 1. The airfoil sections over the outboard two thirds of the sweptwing were cambered. The results of this initial series of tests are reported in Ref. 6; only summary figures are presented in this paper for comparison purposes. The effects of angle of attack and span loadings were investigated at downstream distances of up to 200 span lengths.

The present paper addresses itself primarily to the sweptwing planform fitted with seven flap segments on each half of the span. The flaps were used to achieve desired wingspan loadings. Four different span loadings at a lift coefficient of 0.70 were selected for investigation: 1) the clean wing (no flaps deflected); 2) a typical landing configuration; 3) a configuration tailored to reduce the gradient in the loading at the wingtip; and 4) a configuration with flaps deflected alternately $\pm 15°$ in an attempt to create multiple spanwise span-load gradients (sawtoothing effect in the span-load distribution). These configurations are illustrated in Fig. 2. The flap schedules and test angles of attack to produce a common lift coefficient of 0.70 for all configurations are listed in Table 2. Lift and drag force measurements were obtained for these configurations in the NASA Ames 7- by 10-ft Wind Tunnel prior to the water tank tests. These force measurements were made at the same Reynolds number as the tank tests and are summarized in Fig. 3.

Experimental Procedure

As a means of marking the vortex centerline, a thin sheet of air bubbles was generated across the tank, approximately 1.5m upstream (toward the starting end) of the test section location of the laser instrument. The axial velocity defect in

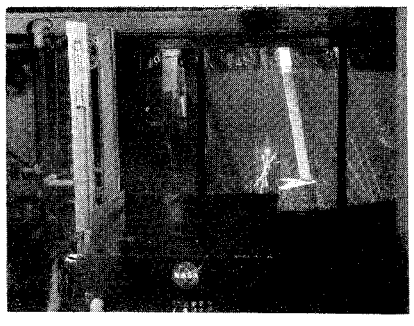

Fig. 1 Installation photograph, swept-wing in the test section of the University of California water tow-tank.

Table 1 Model geometry

	RECTANGULAR WING	DIAMOND WING	SWEPT WING
PLANFORM			
SPAN	61 cm (24 in)	61 cm (24 in)	61 cm (24 in)
REFERENCE CHORD	11.43 cm (4.5 in)	11.43 cm (4.5 in)	10.41 cm (4.1 in)
ASPECT RATIO	5.33	5.33	5.85
ROOT CHORD	11.43 cm (4.5 in)	22.86 cm (9.0 in)	18.21 cm (7.17 in)
LEADING EDGE SWEEP	0°	20.6°	38.6°
TAPER RATIO	1.0	0	0.25
SECTION ROOT	NACA 0015	NACA 0015	NACA 0011-64 (MODIFIED)
TIP	NACA 0015	NACA 0015	NACA 0008-64 (MODIFIED)

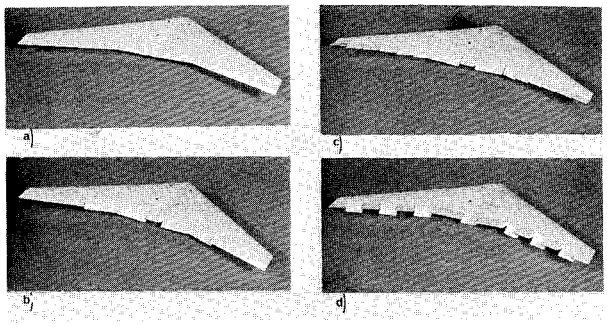

Fig. 2 Swept-wing model test configurations: a) clean configuration; b) landing configuration; c) tailored configuration; d) sawtooth configuration.

Table 2 Swept-wing flap schedule

CONFIGURATION	SEMISPAN FLAP SETTINGS [a] (INBOARD) (OUTBOARD)	C_L	α
CLEAN	0° / 0° / 0° / 0° / 0° / 0° / 0°	.70	6.8°
LANDING	20°/ 20°/ 20°/ 0° / 0° / 0° / 0°	.70	3.4°
TAILORED	10°/ 10°/ 0° /-10°/-15°/-20°/-30°	.70	7.5°
SAWTOOTH	-15°/ 15°/-15°/ 15°/-15°/ 15°/-15°	.70	9.2°

[a] DOWNWARD DEFLECTIONS ARE POSITIVE

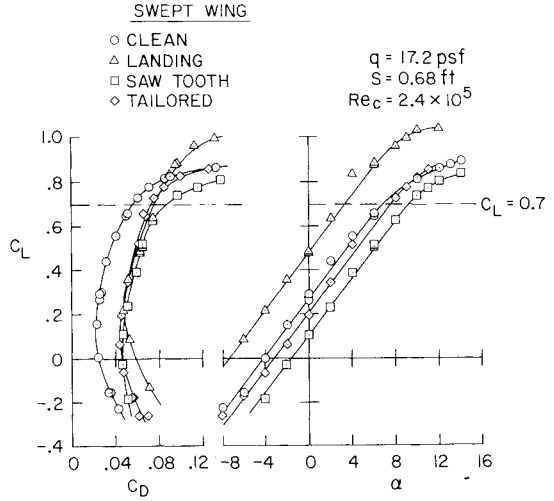

Fig. 3 Lift and drag force characteristics of sweptwing model test configurations.

the vortex core region then acted in such a way as to drag some of these bubbles toward the passing wing; the radial pressure gradient associated with the rotational flow centered the bubbles in single-file, producing a fine string of bubbles along the vortex centerline. As the vortex pair rose, due to mutual interaction, the laser system was raised manually in order to maintain the optical axis in alignment with the vortex centerline. Spanwise continuous traversals of the focal point through the vortex were then made with an automatic scan reversal, which was set to encompass the area of interest (namely, the near vortex and a substantial region on either side of its core). A polystyrene copolymer latex solution was added to the water in the region of the test section to ensure that a sufficient number of scattering particles would be present. The size distribution of these particles was between 2 and 15 μ. The timing for a given run began when the streamlined strut passed through the outgoing laser light at the test station. Several runs were made with test times close to 1 min after passage of the model, or equivalently (for $U_\infty = 2.07$ m/sec) to downstream distances of 200 span lengths.

Data Acquisition and Presentation

Rapid spatial scanning of the trailing vortex flow was accomplished by using a two-dimensional argon-ion laser velocimeter system.[3-6] Use of this two-color (4 beam) technique allowed simultaneous measurement of both the axial and tangential velocities while a vortex was being spatially traversed. The measured frequencies are linearly related to the velocity components of the orthogonal velocities by the following equations:

$$u = \frac{(5145\text{Å})f_x}{2\mu \sin \theta/2} \; ; \; w = \frac{(4880\text{Å})f_z}{2\mu \sin \theta/2}$$

where u and w are velocity components parallel to (positive upstream) and normal to (positive upward) the tank longitudinal centerline, respectively. These expressions represent the vortex axial (V_x) and tangential (V_θ) velocities when a centerline penetration of the vortex is achieved. The measured velocities were not corrected for angularity between the vortex longitudinal centerline and the tank longitudinal centerline resulting from mutual interactions of the vortex pair. For the operating conditions of this test, these corrections are less than three percent of the measured signal and well within the scatter of the data. The angular dependence sin $\theta/2$ is a function of the distance of the crosspoint from the transmitting lens. The velocimeter is hoisted vertically to track the aging vortices as they rise in the tank. The index of refraction for water was used in this test ($\mu = 1.33$). Signal processing was accomplished with two identical spectrum analyzer systems. The vertical (signal energy content) and horizontal (frequency position) outputs of each analyzer were recorded on magnetic tape. Selected traversals could then be transferred to oscillograph paper. Voltages from linear potentiometers, one driven by the scanning lens carriage and the other by the laser hoist carriage were also recorded. These voltages (representing the tank location of the test point) and the frequency information from the spectrum analyzers were processed to yield velocity and spatial position relative to the wing trailing edge.

Vortex maximum velocities, presented as fractions of towing speed U_∞ and location x downstream of the wingtip trailing edge ($x=0$), are normalized to either wing reference chord c or span b. Velocity distributions normalized on towing speed are presented as functions of percent wingspan b for various downstream distances x/b. Maximum tangential velocities represent an average of the inboard and outboard peak tangential velocity from a given velocity distribution.

Discussion of Results

Maximum Tangential Velocities

A summary of vortex maximum tangential velocity as a function of downstream distance for the rectangular wing at angles of attack of 4°, 5°, and 8° is presented in Fig. 4. Also shown in the figure, for comparison, are the results from geometrically similar wings tested in the NASA Ames 40- by 80-ft and 7- by 10-ft Wind Tunnels.[2,4] It is seen that the results from the 40- by 80-ft tunnel (at 10 and 31 span lengths) are in reasonably good agreement with the tow-tank results. The 7- by 10-ft data were obtained quite close to the wing (at 0.38 span lengths) but still show fair agreement with the water-tank data. The data identify two separate flow regions; a "plateau" region where the vortex maximum rotational velocity remains constant after rollup to downstream distances of 25 to 45 span lengths, and then a decay region which persists to the limits of the test distance (approximately 200 span lengths). During the tests, there was concern as to whether the initiation of the velocity decay was a real flow phenomenon or a consequence of starting and stopping waves. This possibility was explored experimentally and analytically and is discussed at length in Ref. 6. It was concluded, however, that the test results were not affected by motion waves. The plateau region did not come as a complete surprise, since its existence is suggested in the turbulent shear-flow calculations of Donaldson.[7] The results indicate that inviscid vortex structure calculations[1] should be applicable to downstream distances as great as 45 spans for rectangular wings at lower coefficients; indeed, Rossow,[8] using an inverse Betz technique, can predict the span loading from measured velocity profiles in this plateau region.

Figure 4 suggests that the duration of the plateau region is reduced as the vortex maximum tangential velocity increases. This, coupled with a nominal decay ratio of $(x/b)^{-1/2}$ results in a far wake structure that appears independent of angle of attack of the generating wing. For convenience in visualizing separation distances, the downstream distance shown in Fig. 4 is also presented in kilometers behind an aircraft with a 61m (200 ft) wingspan. The results indicate that a trailing vortex behind a generating aircraft with a $C_L \leq 0.56$ and a 61m wingspan will not begin to decay until downstream distances of 1.61 km (1 mi) or more are achieved. Iversen,[9] who has correlated this rectangular wing data with other available ground-based and flight data, reports that decay begins at about 12 span lengths or a little over 1/2 km (1/3 mi) behind a generating aircraft with a rectangular wing at a $C_L = 1.0$. Of greater significance, Ref. 9 concludes that for Reynolds num-

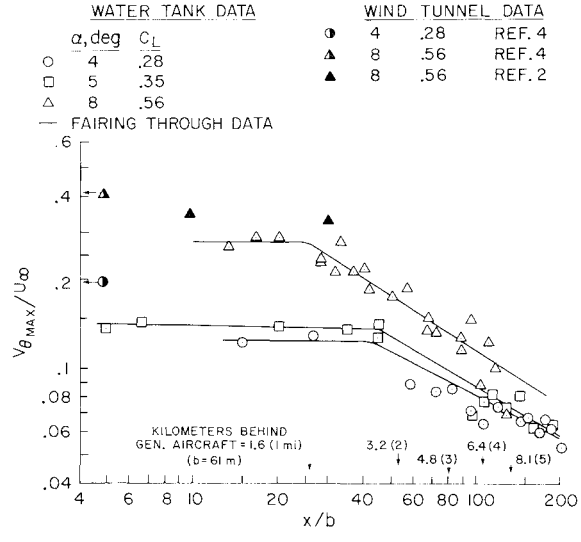

Fig. 4 Variation of rectangular wing maximum tangential velocity with angle of attack and downstream distance. $U_\infty = 2.07$ m/sec.

bers of the order of the present test and greater, the dimensionless maximum tangential velocity is essentially independent of Reynolds number. This finding adds additional credibility to the use of water tank data to predict the vortex characteristics at flight scale.

The effect of wing planform span loading on downstream vortex maximum tangential velocity is summarized in Fig. 5. The results from rectangular, swept, and diamond-shaped planforms at 5° angle of attack and a towing speed of 2.07 m/sec are presented. Reference 6 reports detailed velocity profiles on these configurations. The velocity has been scaled by a normalized circulation

$$\Gamma_0/U_\infty b = \tfrac{1}{2}(C_L/AR)\,b/b_e$$

to minimize effects due to differences in lift coefficient, aspect ratio, and spanwise vortex location. Values used for b/b_e were those measured during the tests. To preserve the decay rate, the downstream distance has been scaled by the same parameters. The dimensionless circulation for each wing is listed in the figure.

With the exception of a clearly defined decay region for the diamond wing planform, once again, plateau and decay regions are identified. The wake rotational characteristics are not significantly different between the elliptically loaded swept-wing and the rectangular wing, a not too surprising result in view of the fact that their span loadings are not radically different. However, the diamond planform wing yields maximum wake tangential velocities less than half those of the rectangular and swept planforms with a plateau region that extends from 80 to 100 span lengths. This reduction in tangential velocity is consistent with the trends predicted by Rossow in Ref. 6. It is a pure span-loading effect caused by the reduced vorticity shed at the wingtip of the diamond wing planform. Figure 5 shows that near field differences in maximum tangential velocity for the three wing planforms become indiscernible in the far field. This is a result of the combination of the shorter plateau regions that are associated with the higher values of maximum tangential velocity and comparable decay rates.

The results obtained by introducing span loading variations on the swept-wing by flap deflections are summarized in Fig. 6. The four configurations shown in Fig. 2 and tabulated in Table 2 were tested at a common lift coefficient of 0.7 and a towing speed of 2.07 m/sec. The tailored configuration was an attempt to reduce the gradient in lift loading at the wingtip (resulting in reduced shed vorticity at the wingtip, similar to the diamond wing planform). The sawtooth configuration was intended to develop multiple spanwise load gradients that produce numerous vortices on each side of the wing, in an attempt to create wake instabilities and mutual interactions to inhibit an orderly wake rollup.

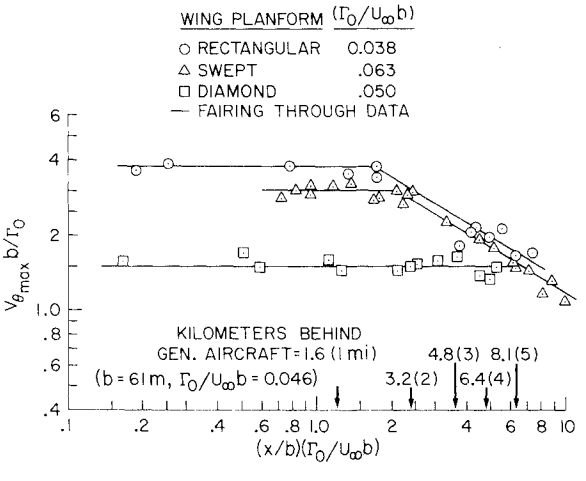

Fig. 5 Effect of wing planform span loading and downstream distance on maximum tangential velocity. $U_\infty = 2.07$ m/sec, $\alpha = 5°$.

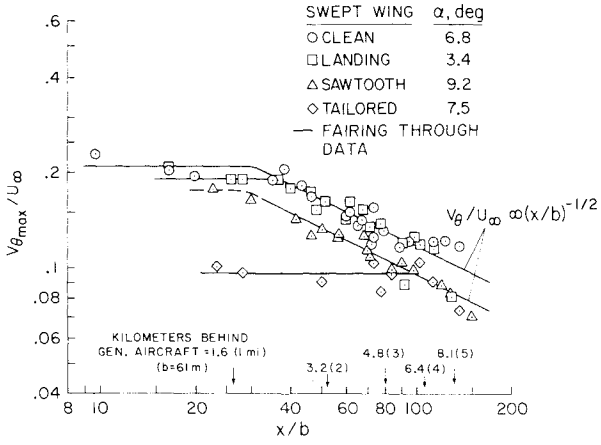

Fig. 6 Effect of sweptwing span loading and downstream distance on maximum tangential velocity. $U_\infty = 2.07$ m/sec, $C_L = 0.7$.

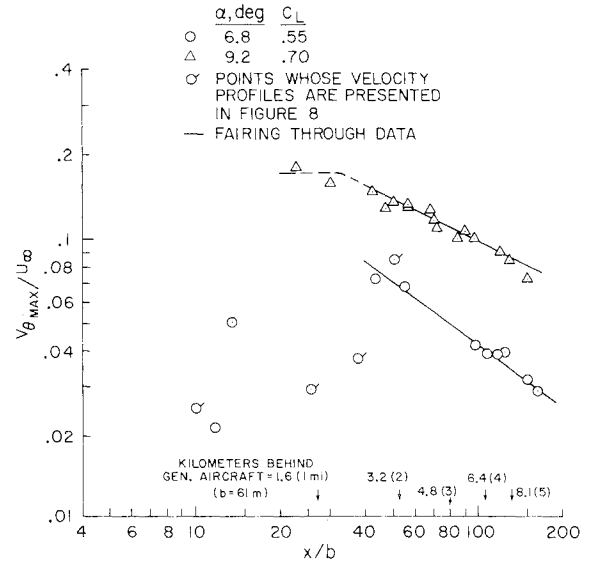

Fig. 7 Variation of sawtooth configuration maximum tangential velocity with angle of attack and downstream distance. $U_\infty = 2.07$ m/sec.

Although the amount of data precludes a positive identification of a plateau region for these flapped configurations, the data suggest its presence. The decay region is readily apparent. Although a plateau region could never really be identified for the sawtooth configuration, the wake did eventually roll-up and achieve rotational velocities almost comparable to the clean and landing configurations at 30 span lengths. At a lift coefficient of 0.7, there is almost no discernible difference in the downstream characteristics of the maximum rotational velocities in the wake of the clean wing or the landing configuration. The results obtained with the tailored configuration are much like those obtained with the diamond wing planform. The maximum wake tangential velocities are less than half those of the other configurations, and the plateau region extends from 80 to 100 span lengths. Once again, however, this long plateau is instrumental in reducing large differences in maximum rotary velocities in the wake at 1.6 km (i mi) behind the wing to insignificant differences in velocity at 6.4 km (2 mi). The faired lines through the data in the decay region have a slope of $-1/2$.

The sawtooth configuration was also tested at a lift coefficient of 9.55, where the ratio of additional to basic lift (lift associated with angle of attack and flap deflection, respectively) makes this approach to vortex alleviation more

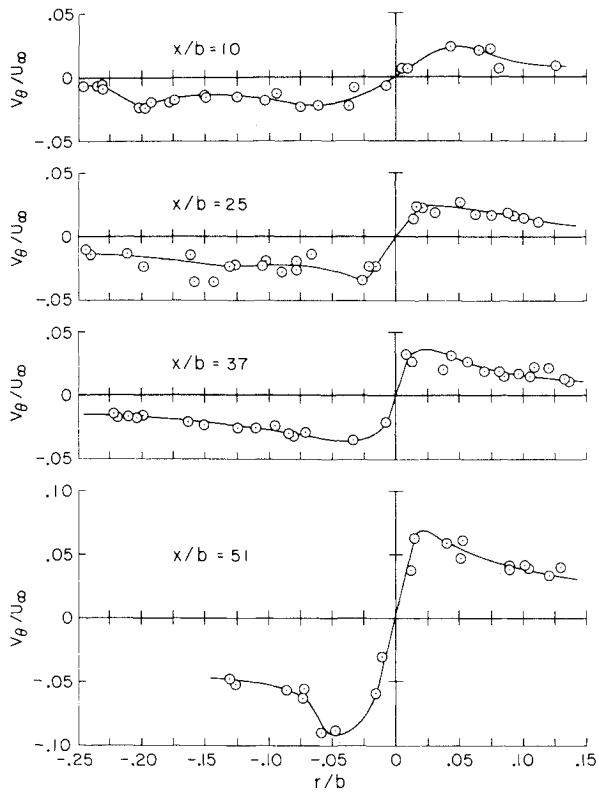

Fig. 8 Sawtooth configuration tangential velocity profile time histories. $U_\infty = 2.07$ m/sec, $\alpha = 6.8°$.

favorable. In Fig. 7, these results are compared to those obtained at a $C_L = 0.7$. In neither case is a plateau region ever identifiable, although a decay region is readily evident. Wake rollup is delayed in each case with a greater delay (to approximately 45 span lengths) at the lower C_L, and what appears to be a greater decay rate is finally established. Flow visualization during the test indicated that several vortices were generated along each half of the wingspan and that these multiple vortices interacted with each other in Crow-like instabilities. After the effect of vortex "looping" or "linking" had subsided, one remaining vortex persisted on each side of the wing and experienced a decrease in diameter and an increase in rotational velocity. This is the vortex whose maximum tangential velocities are presented in Fig. 7. Figure 8 presents the tangential velocity profiles for the flagged maximum velocity points of Fig. 7. This graphically illustrates the core tightening and rotational velocity speedup of the remaining vortex. The effect of the number of flaps, their size, and deflection schedule was not explored to see if a further delay or elimination of an orderly wake rollup might allow utilization of this technique at higher lift coefficients.

Tangential Velocity Profiles

A comparison of the complete tangential velocity profiles for each of the sweptwing configurations as measured at 25 span lengths is presented in Fig. 9. At this downstream location, all of the configurations, with the possible exception of the sawtooth configuration, are in the plateau region. Although the sawtooth configuration never reached an identifiable maximum tangential velocity plateau because of a delayed rollup, at 25 span lengths it appears to be very close to a plateau (Fig. 6). Since the tangential velocities are insensitive to downstream distance in this region, differences in the velocity profiles are a result of differences in span loading rather than turbulent decay. It is seen that the tailored configuration yields lower rotational velocities in the core and adjacent regions and has a more diffuse velocity profile. Both of these features are desirable from the standpoint of vortex

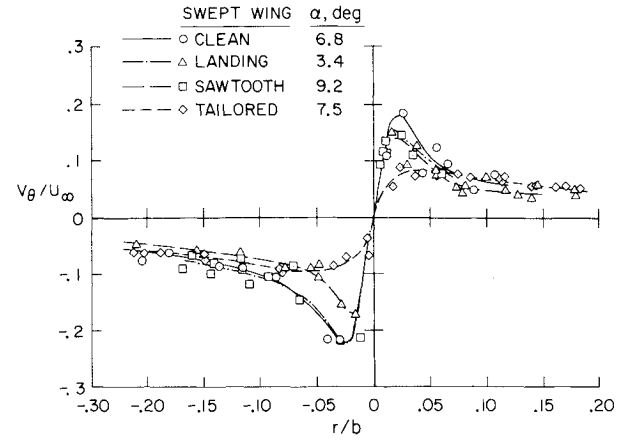

Fig. 9 Comparison of sweptwing configuration tangential velocity profiles. $U_\infty = 2.07$ m/sec, $C_L = 0.7$, $x/b = 25$.

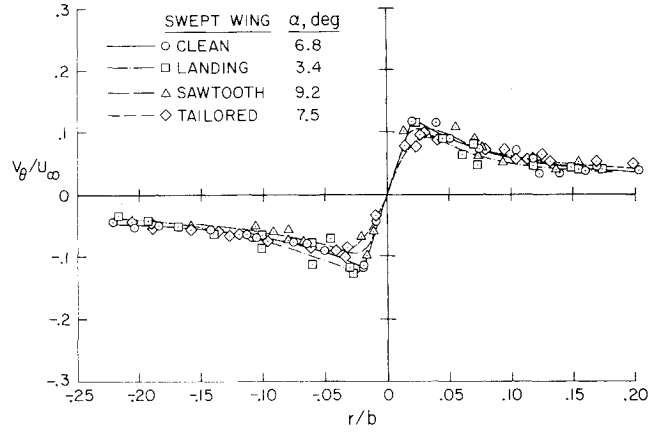

Fig. 10 Comparison of sweptwing configuration tangential velocity profiles. $U_\infty = 2.07$ m/sec, $C_L = 0.7$, $x/b = 95$.

hazard alleviation, although the velocity profile should be integrated along the span of a following wing to evaluate the upset tendencies before any final assessment of alleviation can be made.

At 95 span lengths downstream, in the decay region, the tangential velocity profiles are quite similar (Fig. 10). Within the scatter of the data, the dependence of the velocity profile on wingspan loading has lost most of its significance. In contrast to Fig. 9, the clean, landing, and sawtooth configurations have decayed to comparable levels with the tailored span loading at this far field location. Figure 11a shows the insensitivity of tangential velocity to downstream distance for both the diamond wing planform and the tailored configuration. The velocity bands presented represent the superposition of data from 22 to 98 spans for the diamond planform and 26 to 86 spans for the tailored configuration. It has been shown above that both of these configurations yield greatly suppressed tangential velocities, lower concentrations of vorticity in the core, and extended plateau regions as compared to any of the other configurations tested. Figure 11b shows the normalized span loading of these wings; these values were calculated using the vortex-lattice method of Hough.[10] Also shown for the diamond wing planform is the tip loading obtained from the measured velocity profiles by using the inverse Betz calculations from Rossow.[8] The discrepancy between the vortex-lattice, and the inverse Betz results near the wingtip is believed to be due to the influence of the vortex viscous core in the inverse Betz calculations. Viscous effects are not accounted for in the vortex-lattice theory. Reference 8 shows that the vortex-lattice predictions for the tailored configurations are representative of those ob-

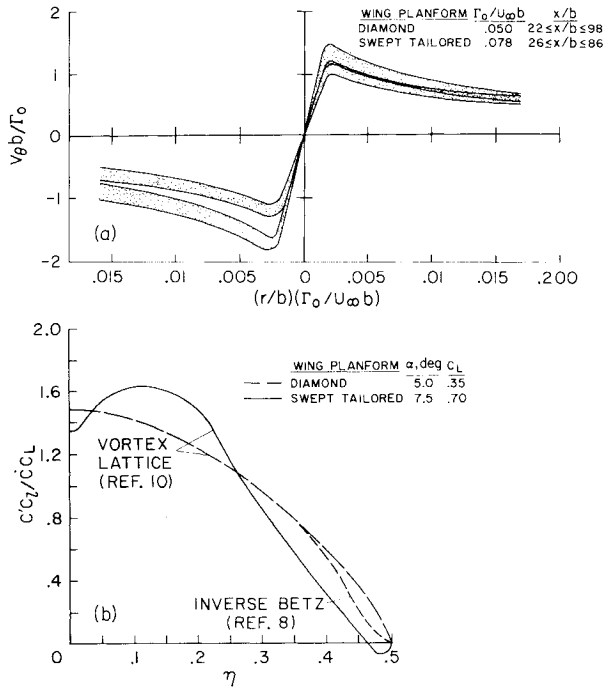

Fig. 11 Comparison of diamond planform and tailored sweptwing: a) tangential-velocity-profile time histories; b) predicted normalized span loadings. $U_\infty = 2.07$ m/sec.

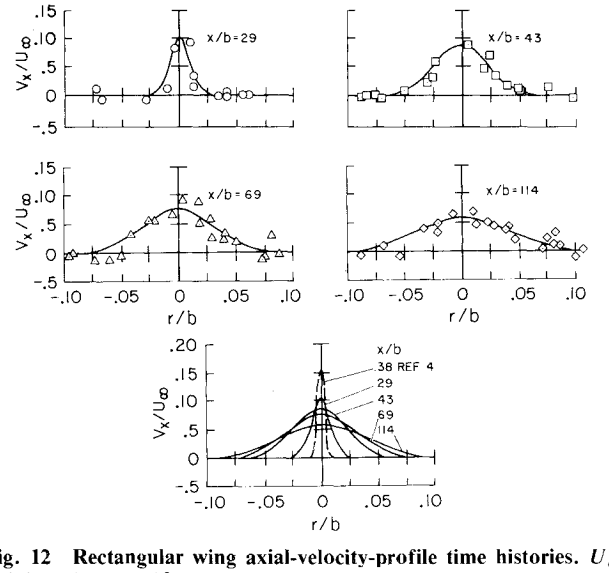

Fig. 12 Rectangular wing axial-velocity-profile time histories. $U_\infty = 2.07$ m/sec, $\alpha = 8°$.

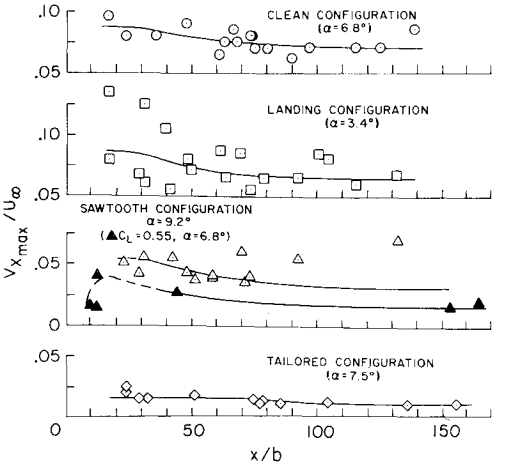

Fig. 13 Effect of sweptwing span loading and downstream distance on maximum axial velocity. $U_\infty = 2.07$ m/sec, $C_L = 0.7$.

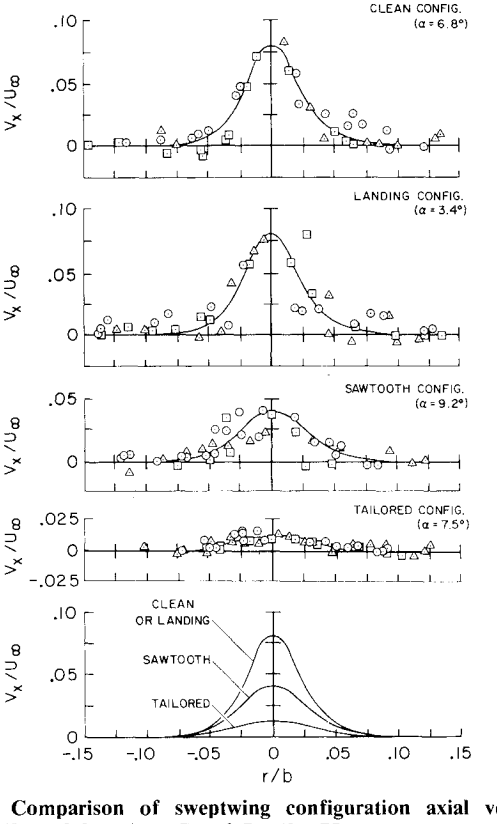

Fig. 14 Comparison of sweptwing configuration axial velocity profiles. $U_\infty = 2.07$ m/sec, $C_L = 0.7$, $x/b = 75$.

tained from the inverse Betz method and are not included here. The tips of the diamond planform wing were unloaded due to its planform; the tailored wing had its tips unloaded by spanwise flap deflections. The net effect on the wake is comparable. Hence, altering the span loading by either planform or flap deflection to unload the outboard sections of the wing is equally effective in reducing the wake rotational velocities and broadening the vortex core.

Axial Velocities

The existence of axial flow in the cores of lift-generated trailing vortices has been established experimentally[4-6,11-15]; both defects and enhancements of the axial velocity were reported. The present series of tests were designed to obtain continuous axial-velocity data from the near field into the far field for a range of wingspan loadings. The results showing variation of maximum axial velocity defect (flow in the same direction as the model being towed) with downstream distance, for the rectangular wing at 4°, 5°, and 8° angle of attack and a towing speed of 2.07 m/sec has been reported in Ref. 11. These measured velocities show good agreement with near field wind-tunnel data[4,12] and a decrease in maximum axial velocity with both downstream distance and angle of attack for the rectangular wing. A comparison of axial-velocity-profile time histories for this rectangular wing at 8° angle of attack is presented in Fig. 12. These results characterize the radial diffusion of the axial velocity defect in the decay region. A profile obtained in the near field[4] ($x/b = 0.38$) has been included to emphasize the extent to which the momentum is initially concentrated. The diffusive nature of the axial structure is clearly documented, and it is from fairings such as these that the core velocity along the axis can be extracted and its subsequent decay considered.

The downstream variation of the maximum axial velocity defect for the sweptwing configuration is summarized in Fig. 13. The axial velocity is coupled to the tangential velocity

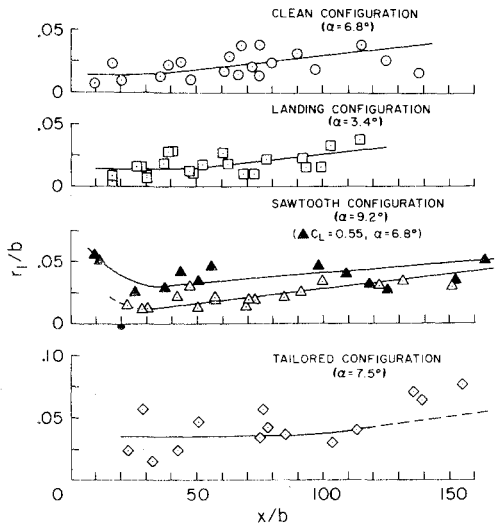

Fig. 15 Effect of sweptwing span loading and downstream distance on core radius. $U_\infty = 2.07$ m/sec, $C_L = 0.7$.

through the downstream variation of centrifugal force. Far-field maximum tangential velocities of all sweptwing configurations are comparable, hence, relative differences in plateau-region values of maximum tangential velocity should be reflected in relative differences in maximum axial velocity. An inspection of Figs. 6 and 13 shows this to be true. The continual slowing down of the tangential velocity in the decay region (leading to a positive axial pressure gradient) and the resulting loss of axial velocity are seen in Fig. 13. There is some uncertainty as to the variation of axial velocity in the far field for the sawtooth configuration due to the lack of axial data in this region. The radial distribution of axial velocity for these sweptwing configurations at 75 span lengths is presented in Fig. 14.

Core Radius

The growth of the core radius with downstream distance for the sweptwing configurations is shown in Fig. 15. The normalized core radius r_1/b is the radius at which the peak tangential velocity occurs in the tangential velocity profile. The positive axial pressure gradient in the decay region results in the increase in core radius, which is evident in Fig. 15 and which is compatible with the axial velocity deceleration shown in Fig. 13. The increase in core radius due to the delayed rollup of the sawtooth configuration in the near field is also shown. Figure 15 suggests a nominal core growth that is proportional to the square root of the downstream distance (with the exception of some uncertainty in the core growth of the tailored configuration). It has been shown previously (Fig. 6) that the tangential velocity decays as $(x/b)^{-1/2}$, and now it has been established that the core is growing as $(x/b)^{1/2}$, which implies that the aging vortex is maintaining a geometric similarity.[16] As an example of this similarity condition, if the faired curve through the clean swept-wing data of Fig. 6 is used in conjunction with the faired curve through the data of Fig. 15, it is found that circulation within the core region remains constant $[(V_{\theta_{max}}/U_\infty)(r_1/b) \simeq 0.0034]$ over the range of downstream distances tested.

Conclusions

The experimental results of this study identify two characteristic flow regions for the dependence of vortex maximum tangential velocity on downstream distance. The first, a region of constant velocity, can extend from rollup to 100 span lengths, depending on span loading and angle of attack. This is followed by a decay region where $V_{\theta_{max}}$ varies as $(x/b)^{-1/2}$. This implies that inviscid vortex structure calculations should be applicable to distances as great as 100 span lengths downstream for certain wing configurations.

It is shown that tailoring the wingspan loading by either planform or flap deflection (to reduce wingtip vorticity by unloading the outboard sections of the wing) is equally effective in reducing the wake rotational velocities by factors of 2, broadening the vortex core, and extending the plateau region to 100 span lengths.

An orderly wake rollup was delayed to 45 span lengths downstream by introducing multiple vortices along the wingspan with alternate up-down flap deflections. These multiple vortices interacted with each other in Crow-like instabilities. A plateau region was never achieved for this configuration.

Over the range $10 \leq x/b \leq 150$, the swept-wing configuration maximum tangential velocity $V_{\theta_{max}}/U_\infty$ was 0.21 to $x/b = 32$, and then decayed to 0.095 while circulation in the core remained constant. Factors of two differences in $V_{\theta_{max}}/U_\infty$ in the near field, because of differences in angle of attack or span loading, became insignificant in the far field as a result of the initially higher values of $V_{\theta_{max}}/U_\infty$ having shorter plateau regions but similar decay rates.

Agreement is shown between the present measurements and those obtained in the near field in wind tunnels. Data from the present test has been correlated[9] with other ground-based experiments and flight data, and it is concluded that, for Reynolds numbers of the order of the present test and greater, the vortex maximum tangential velocity is nearly independent of Reynolds number. This finding adds additional credibility to the use of water tank data to predict the vortex characteristics at flight Reynolds number.

References

[1] Rossow, V. J., "Theoretical Study of Lift-Generated Vortex Sheets, Designed to Avoid Roll Up," TM X-62,304, Sept. 1973, NASA.

[2] Corsiglia, V. R., Schwind, R. G., and Chigier, N. A., "Rapid Scanning, Three-Dimensional Hot-Wire Anemometer Surveys of Wing-Tip Vortices," *Journal of Aircraft*, Vol. 10, Dec. 1973, pp. 752-757.

[3] Grant, G. R. and Orloff, K. L., "A Two-Color, Dual Beam Backscatter Laser Doppler Velocimeter," TM X-62,254, March 1973, NASA.

[4] Orloff, K. L. and Grant, G. R., "The Application of Laser Doppler Velocimetry to Trailing Vortex Definition and Alleviation," TM X-62,243, Feb. 1973, NASA.

[5] Ciffone, D. L., Orloff, K. L., and Grant, G. R., "Laser Doppler Velocimeter Investigation of Trailing Vortice Behind a Semispan Swept Wing in a Landing Configuration," TM X-62,294, Aug. 1973, NASA.

[6] Orloff, K. L., Ciffone, D. L., and Lorincz, D., "Airfoil Wake Vortex Characteristics in the Far Field," TM X-62,318, Nov. 1973, NASA.

[7] Donaldson, C. DuP., "Calculation of Turbulent Shear Flows for Atmospheric and Vortex Motions," *AIAA Journal*, Vol. 10, Jan. 1972, pp. 4-12.

[8] Rossow, V. J., "Prediction of Span Loading from Measured Wake-Vortex Structures—An Inverse Betz Method," TM X, NASA (to be published).

[9] Iversen, J. D., "Correlation of Turbulent Trailing Vortex Decay Data," *Journal of Aircraft* (to be published).

[10] Hough, G., "Remarks on Vortex-Lattice Methods," *Journal of Aircraft*, Vol. 10, May 1973, pp. 314-317.

[11] Ciffone, D. L. and Orloff, K. L., "Axial Flow Measurements in Trailing Vortices," *AIAA Journal*, Vol. 12, Aug. 1974, pp. 1154-1155.

[12] Chigier, N. A. and Corsiglia, V. R., "Wind Tunnel Studies of Wing Wake Turbulence," *Journal of Aircraft*, Vol. 9, Dec. 1972, pp. 820-825.

[13] Logan, A. H., "Vortex Velocity Distributions at Large Downstream Distances," *Journal of Aircraft*, Vol. 8, Nov. 1971, pp. 930-932.

[14] Olsen, J. H., *Aircraft Wake Turbulence and Its Detection*, edited by J. H. Olsen, A. Goldberg and M. Rogers, Plenum Press, New York, 1971, p. 455.

[15] Lezius, D. K., "Study of the Far Wake Vortex Field Generated by a Rectangular Airfoil in a Water Tank," TM X-62,274, May 1973, NASA.

[16] McCormick, B. W., Tangler, J. L., and Scherrib, H. E., "Structure of Trailing Vortices," *Journal of Aircraft*, Vol. 5, March 1968, pp. 260-267.